Magnetic-tunnelling-induced Weyl node annihilation in TaP

Cheng-Long Zhang[1], Su-Yang Xu[2], C. M. Wang[3,4], Ziquan Lin[5], Z. Z. Du[3,6], Cheng Guo[1], Chi-Cheng Lee[7,8], Hong Lu[1], Yiyang Feng[1], Shin-Ming Huang[7,8,9], Guoqing Chang[7,8], Chuang-Han Hsu[7,8], Haiwen Liu[1], Hsin Lin[7,8], Liang Li[5], Chi Zhang[1,10], Jinglei Zhang[11], Xin-Cheng Xie[1,10], Titus Neupert[12], M. Zahid Hasan[2], Hai-Zhou Lu[3]★, Junfeng Wang[5]★ and Shuang Jia[1,10]★

Weyl nodes are topological objects in three-dimensional metals. Whereas the energy of the lowest Landau band of a conventional Fermi pocket increases with magnetic field due to the zero-point energy ($1/2\hbar\omega$), the lowest Landau band of Weyl cones stays at zero energy unless a strong magnetic field couples Weyl fermions of opposite chirality. In the Weyl semimetal TaP, which possesses two types of Weyl nodes (four pairs of W1 and eight pairs of W2 nodes), we observed such a magnetic coupling between the electron pockets arising from the W1 Weyl fermions. As a result, their lowest Landau bands move above the chemical potential, leading to a sharp sign reversal in the Hall resistivity at a specific magnetic field corresponding to the separation in momentum space of the W1 Weyl nodes, $\sqrt{(eB/\hbar)} \sim \Delta k_{W1}$. By contrast, annihilation is not observed for the hole pocket because the separation of the W2 Weyl nodes is much larger. These findings reveal the nontrivial topology of Weyl fermions in high-field transport measurements and demonstrate the observation of Weyl node annihilation, which is a unique topological phenomenon associated with Weyl fermions.

U nderstanding electronic properties under a high magnetic field has been a fertile ground for discovering new physics. Historically, in various types of two-dimensional electron gases (2DEG), researchers have discovered novel phases, including the fractional quantum Hall effect (FQHE)[1,2] or Wigner crystals[3], under an intense magnetic field. In a 3D metal, a magnetic field leads to the formation of a Landau band (LB) spectrum. The ultra-quantum limit refers to a condition where, at a sufficiently high magnetic field, all higher LBs are pushed away from the Fermi level whereas only the lowest Landau band (LLB) crosses the chemical potential. Unfortunately the ultra-quantum limit can be accessed only in a limited number of materials under a moderate magnetic field, as it requires the carrier density to be sufficiently low. Previously, the ultra-quantum limit was achieved in a few topologically trivial materials such as lightly doped semiconductors[4,5] and certain compensated semimetals, including graphite, bismuth, and silver selenide (Kramers Weyl points are far away from the experimental Fermi level)[6–9]. A number of very interesting phenomena were discovered[6–14].

The recently discovered topological Weyl semimetals in the TaAs family[15–24] open up a new territory along this direction. In contrast to a conventional metal/semimetal, the metallicity of a Weyl semimetal is guaranteed by the presence of Weyl nodes. The Weyl

nodes, which arise from the crossings between the conduction and valence bands, are topological objects in a 3D band structure. In the presence of translational symmetry, they cannot be removed unless pairs of Weyl nodes of opposite chirality are moved together to annihilate each other. The Weyl node annihilation is a unique topological phenomenon associated with Weyl fermions. Although angle-resolved photoemission spectroscopy (ARPES) has revealed the linear dispersion of the Weyl cones and previous quantum oscillation measurements have studied high Landau bands[22,25], the topological character of the Weyl fermion is reflected by the unique properties of its LLB, as described below, which remains unexplored. Equally importantly, ARPES and other experiments have not observed the annihilation of the Weyl nodes. In this paper, we make an attempt to understand how these nontrivial topological properties of a Weyl semimetal affect its transport properties in the ultra-quantum limit. In particular, we study a Landau physics phenomenon—magnetic tunnelling—where LBs from adjacent Fermi pockets hybridize, leading to new features in the quantum oscillation. The magnetic tunnelling of LLBs has never been observed because, in the few existing semimetals where LLBs can be accessed (bismuth and graphite[6–8,10–13]), the pockets are far separated in k space so that magnetic tunnelling is negligibly small. Here, we report the observation of magnetic tunnelling of the LLBs

[1]International Center for Quantum Materials, School of Physics, Peking University, Beijing 100871, China. [2]Laboratory for Topological Quantum Matter and Spectroscopy (B7), Department of Physics, Princeton University, Princeton, New Jersey 08544, USA. [3]Institute for Quantum Science and Engineering and Department of Physics, South University of Science and Technology of China, Shenzhen 518055, China. [4]School of Physics and Electrical Engineering, Anyang Normal University, Anyang 455000, China. [5]Wuhan National High Magnetic Field Center, Huazhong University of Science and Technology, Wuhan 430074, China. [6]School of Physics, Southeast University, Nanjing 211189, China. [7]Centre for Advanced 2D Materials and Graphene Research Centre National University of Singapore, 6 Science Drive 2, Singapore 117546, Singapore. [8]Department of Physics, National University of Singapore, 2 Science Drive 3, Singapore 117542, Singapore. [9]Department of Physics, National Sun Yat-Sen University, Kaohsiung 804, Taiwan. [10]Collaborative Innovation Center of Quantum Matter, Beijing 100871, China. [11]Anhui Province Key Laboratory of Condensed Matter Physics at Extreme Conditions, High Magnetic Field Laboratory of the Chinese Academy of Sciences, Hefei 230031, Anhui, China. [12]Department of Physics, University of Zurich, Winterthurstrass 190, CH-8052 Zurich, Switzerland. *e-mail: luhz@sustc.edu.cn; jfwang@hust.edu.cn; gwljiashuang@pku.edu.cn
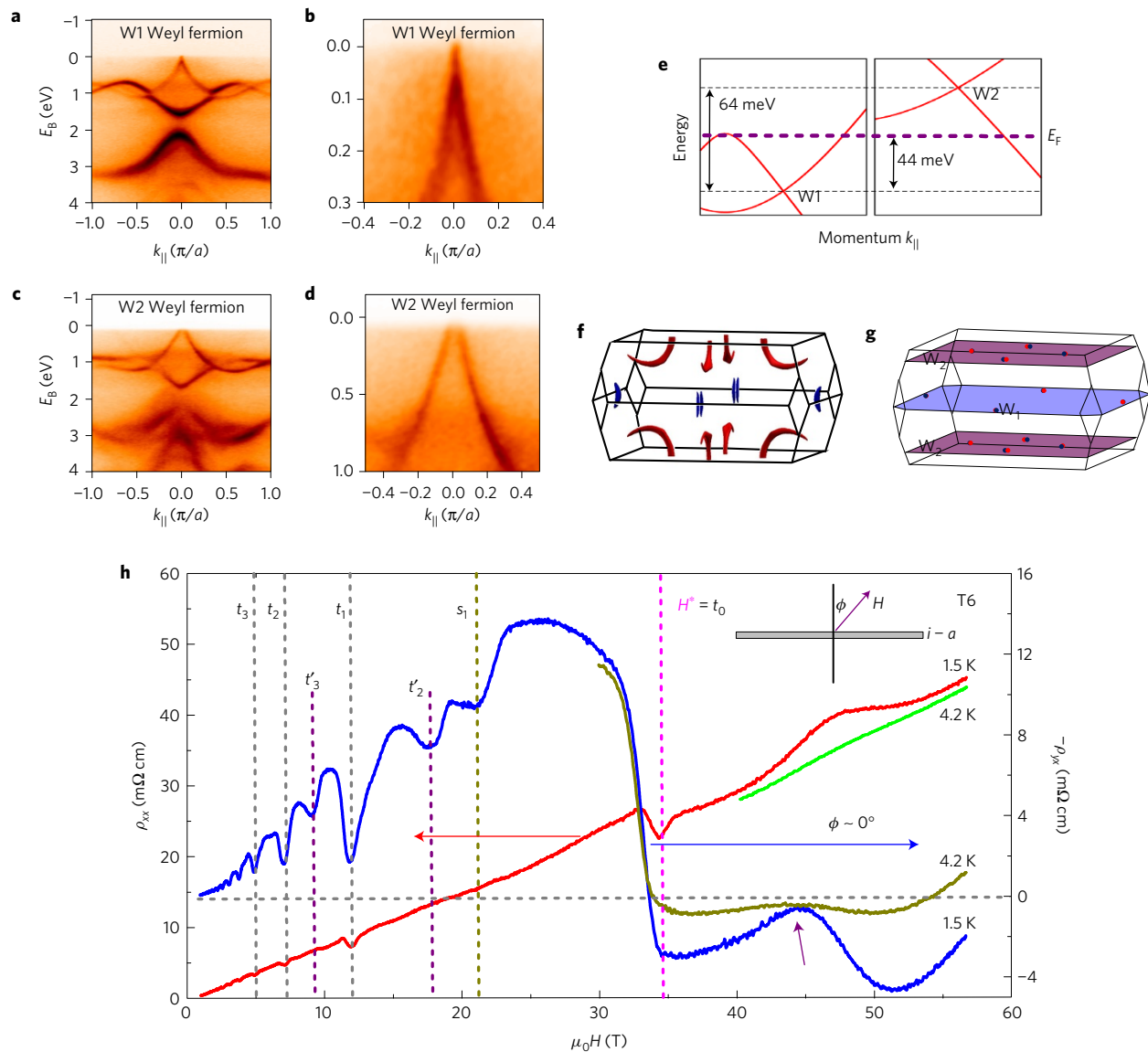
Figure 1 | Weyl Fermions in TaP and its anomaly at high magnetic field. a–d, ARPES measurements of band dispersions near W1 and W2 Weyl nodes. The E–k dispersion of the W1 Weyl fermions (**a,b**) was taken with a photon energy of 610 eV, whereas the E–k dispersion of the W2 Weyl fermions (**c,d**) was taken with a photon energy of 650 eV. **e**, Electron and hole pockets in a reduced unit cell. **f,g**, The locations of W1 and W2 in the projected k_x–k_y plane in momentum space. **h**, ρ_{xx} and ρ_{yx} versus magnetic field H at 1.5 K and 4.2 K (data in selected field range). The SdH oscillations in ρ_{yx} are more significant than those in ρ_{xx}, while both quantities show dips at the same fields for the SdH oscillations. The dips are associated with two main frequencies (17.3 T and 36.7 T), corresponding to the electron-like ('t') and hole-like ('s') pockets, respectively. With the relation $\rho_{xx} > -\rho_{yx}$, the dips are attributed to the peaks of the density of states (DOS) in the centre of each LB from different bands. All of the dips of $-\rho_{yx}$ were indexed with the letters t, t' (double frequency) and s. The subscripts denote the LB indices. The anomaly indicated by a purple arrow at 44 T shows a strong temperature dependence in the low-temperature region.

in any material irrespective of its topological nature. Furthermore, we show that the magnetic tunnelling of the LLBs in TaP reveals the nontrivial topology of Weyl fermions in high-field measurements.

For a trivial pocket, its LB spectrum can be understood as a series of parabolic bands. The energy at the vertex is given by $E^n = (n + (1/2))\hbar\omega_c$, where n represents the nth LB and ω_c is the cyclotron frequency ($\omega_c = eB/m_c$, m_c is the cyclotron mass). The LLB (E^0) has a finite energy, the zero-point energy $(1/2)\hbar\omega_c$, which increases with magnetic field. By contrast, for a Weyl fermion cone, its LLB is a one-dimensional chiral mode that connects the gap separating the higher LBs. At the Weyl node ($k = k_{Weyl}$), the energy of a LB is given by $E^n = \mathrm{sgn}(n)\sqrt{2e\hbar v_F^2|n|B}$, where v_F is the effective Fermi velocity near the Weyl nodes. Therefore, the energy of the LLB at $k = k_{Weyl}$ is always zero. Since Weyl nodes come in pairs of opposite

topological charge in crystalline systems, the LLBs for a pair of Weyl nodes are two counter-propagating chiral modes connecting the energy gap (for detailed discussion on the difference of various Landau bands, see Supplementary Section I). Therefore, pushing the LLBs away the Fermi level is possible only if a gap opens at their crossing point. How such a gap opens and how it affects the high-field transport signals are unexplored in experiments, which are the subject of this work.

We first present basic information and characterizations necessary for our experiments. Tantalum monophosphide, TaP, crystallizes in a body-centred tetragonal structure without inversion symmetry. TaP possesses two types of Weyl nodes, four pairs of W1 on the $k_z = 2\pi/c$ (c is the lattice constant) plane and the other eight pairs of W2 that are away from this plane[20,21]. ARPES experiments
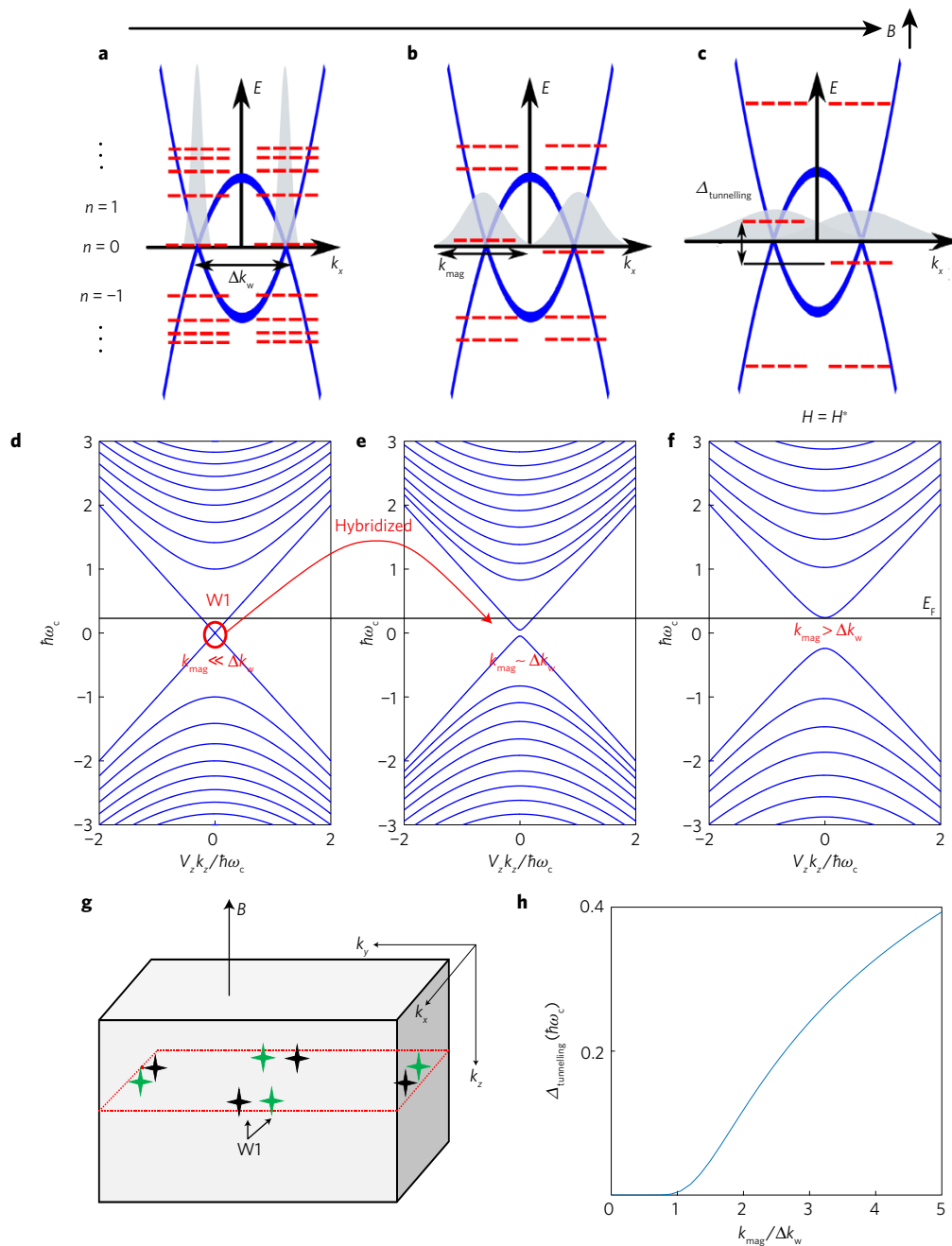
Figure 2 | Mechanism of the gap opening and Weyl node annihilation. a–c, Simple sketches showing the process of hybridization of LBs at higher fields. Solid blue lines show the W1 band structure in the k_x–k_y plane. Dashed lines represent the energy levels of the LBs, n is the LB index, Δk_W is the momentum spacing of W1 nodes of opposite chirality, and k_{mag} is the inverse of the magnetic length. The grey shaded areas are the wavefunction of the Weyl nodes in k_x space. In the absence of an out-of-plane magnetic field B_z, k_x is a good quantum number. Hence the wavefunction of the electron occupying the state of a Weyl node has a definitive k_x eigenvalue. Upon the inclusion of B_z, the translation symmetry along k_x is broken. Hence the wavefunction is broadened into a finite peak in k_x, as schematically shown by the grey peaks here. When quantities k_{mag} and Δk_W become comparable, a sizable gap Δ opens. **d–f**, The LB spectra based on a toy model where pairs of Weyl nodes of opposite chirality are located on the $k_z = 0$ plane. We show the LB spectra at three magnetic fields whose inverse magnetic length, $k_{mag} = \sqrt{eB/\hbar}$, is much smaller than, comparable to, or larger than the Weyl node separation Δk_{Weyl}. **g**, The Weyl node distribution for the toy model, based on which the LB spectra (**d–f**) were calculated. In this model, we have pairs of Weyl nodes located on the same $k_z = 0$ plane. **h**, Evolution of the tunnelling gap opened at the crossing between the LLBs ($\Delta_{tunnelling}$) as the ratio between the two crucial momentum quantities, $k_{mag}/\Delta k_W$.

(Fig. 1a–d) carried out on our TaP samples not only confirm the existence of the two types of Weyl nodes, but also show that the Fermi level is above the W1 Weyl nodes but below the W2 Weyl nodes. Indeed, these ARPES observations are consistent with the theoretical calculations, which show that the calculated Fermi level is 44 meV above W1 (ref. 26). As shown in Fig. 1f, the W1

Weyl fermion cones contribute eight banana-shaped electron-like pockets, whereas the W2 Weyl fermion cones lead to the eight sea-horse-shaped hole-like pockets. Further, the momentum space separation of the W1 nodes is $\Delta k_{W1} = 0.021$ Å^{-1}, whereas the separation of the W2 nodes is much larger, $\Delta k_{W2} = 0.061$ Å^{-1}. These findings in ARPES and band structure calculations suggest
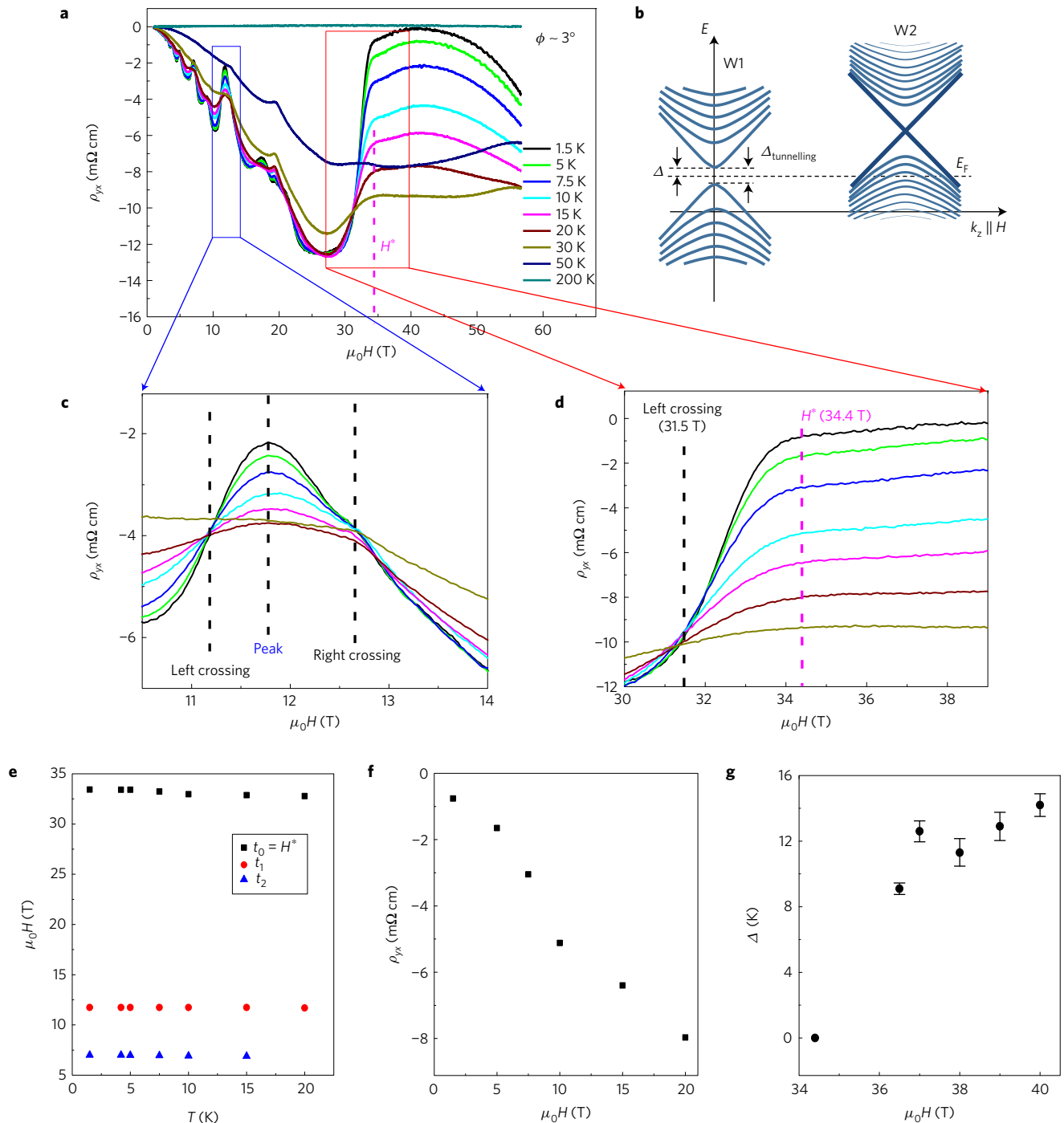
Figure 3 | Temperature-dependent magneto-transport of TaP. a, ρ_{yx} as a function of the magnetic field μ_0H at different temperatures. **b**, A schematic illustration for the LLBs at $H > H^*$. Δ represents the gap between E_F and the bottom of the electron-like LLBs. $\Delta_{tunnelling}$ represents the full gap opened by magnetic tunnelling at high fields. At the same time, E_F still cuts inside the hole-like LLBs. Therefore, only the electron-like carriers show an activation type of behaviour. **c**, Zoom-in around t_1. **d**, Zoom-in around H^*. **e**, Temperature dependence of t_2, t_1 and $H^* = t_0$. t_2, t_1 and $H^* = t_0$ do not show a strong temperature dependence, consistent with the single-particle LB physics. **f**, Temperature dependence of ρ_{yx} at H^* showing strong temperature dependence. **g**, Gap Δ versus B showing the existence of an activation gap for the electron-like carriers. The error bars were obtained from the standard deviations when fitting $n_e - n_h$ as a function of temperature via the activation behaviour. The details of this analysis are shown in the Supplementary Information.

that the Fermi surface of TaP consists of identical hole-like pockets arising from the W2 Weyl fermion cones, and identical electron-like pockets arising from the W1 Weyl fermion cones. The sample that we mainly described in this paper is the sample T6 studied in ref. 27, although other samples with slightly different Fermi level show similar properties (see Supplementary Fig. 2). Indeed, low-field transport measurements[27] yield the following observations, in

agreement with ARPES and calculations. First, low-field (see ref. 27) Hall measurements also show the coexistence of electron-like and hole-like Fermi pockets with almost identical carrier densities ($n_e = 7.5 \times 10^{17}$ cm^{-3}/per pocket, $n_h = 7.2 \times 10^{17}$ cm^{-3}/per pocket). Second, the analysis of the low-field Shubnikov–de Haas (SdH) oscillations (Supplementary Fig. 8a and ref. 27) reveals frequencies of 17.3 T and 36.7 T for the extremal cross-sectional

area of the electron-like pockets (the W1 Weyl fermions 't' here) and hole-like pockets (the W1 Weyl fermions 's' here). Third, we label LB indices 't_n' as the fields at which E_F cuts at the bottom of the nth LB. We identify 't_n' by finding the peak of the longitudinal conductivity σ_{xx} (refs 7,28–30). Last, we further find that the LB fan diagram shows extrapolation around 0, indicating that the electron-like pockets arise from gapless band crossings in three dimensions, consistent with the existence of Weyl fermions (see Supplementary Section V and Supplementary Fig. 8e for more details).

We now present the high-field data (Fig. 1h). We see that the Hall resistivity ρ_{yx} exhibits a sharp sign reversal at a magnetic field located well inside the ultra-quantum limit. Specifically, the Hall resistivity at low fields shows a negative linear field-dependent background until it reaches a plateau at 25 T. Following the plateau, ρ_{yx} flips from negative to positive in a narrow range of 3 T, accompanied by a slope change in ρ_{xx} (Fig. 1h). We denote the field at which ρ_{yx} reaches maximum immediately after the step-like feature as H^* ($H^* = 34.4$ T). At $H > H^*$, a bump-like feature emerges at 44 T in both ρ_{xx} and ρ_{yx} (indicated by an arrow in Fig. 1h). This feature at 44 T is highly sensitive to temperature, as it becomes hardly observable at 4.2 K. The highly temperature-sensitive nature of the 44 T feature suggests a possible many-body interaction, which will not be discussed in detail in this paper. Here we focus on the most striking sign-reversal feature at the field $H^* = 34.4$ T.

We explain the physical process that leads to a gap opening for the LLBs of the Weyl fermions. We consider pairs of Weyl nodes located on the same (k_x, k_y) plane (in this case $k_z = 0$) and a magnetic field along the $\hat{z}$ direction (Fig. 2g). Their LLBs are counter-propagating states that cross at $k_z = 0$, as shown in Fig. 2d. We now ask whether these two counter-propagating chiral modes are allowed to hybridize and open up an energy gap. In the absence of a magnetic field, both energy E and momentum $\mathbf{k}$ are good quantum numbers. We label the wavefunction of a specific Weyl node by its E and $\mathbf{k}$ eigenvalues as $\Psi_{E_{\mathrm{Weyl}}, \mathbf{k}_{\mathrm{Weyl}}}$. The inclusion of an out-of-plane magnetic field B_z breaks the translational symmetry along the k_x and k_y directions. Hence the Weyl node's wavefunction can only be labelled by its E and k_z eigenvalues $\Psi_{E_{\mathrm{Weyl}}, k_z = 0}$. With a small B_z (Fig. 2a), the wavefunction is broadened into a finite peak centred at the k_x value that corresponds to the Weyl node with zero field. As one increases B_z (Fig. 2b,c), the broadening becomes more significant. The broadening can be measured by the inverse of the magnetic length, $k_{\mathrm{mag}} = l_{\mathrm{mag}}^{-1} = \sqrt{eB/\hbar}$, where e is the electron charge, and $\hbar$ is the Planck constant. We compare k_{mag} with the Weyl node separation Δk_{Weyl}. At small fields, the wavefunction broadening is much smaller than the separation of the Weyl nodes ($k_{\mathrm{mag}} \ll \Delta k_{\mathrm{Weyl}}$). Hence the magnetic tunnelling gap ($\Delta_{\mathrm{tunnelling}}$) is negligibly small (Fig. 2a). Only when B_z is sufficiently large, so that the broadening becomes comparable to the separation, $k_{\mathrm{mag}} \sim \Delta k_{\mathrm{Weyl}}$, does a significant gap start to open up (Fig. 2b,c). Figure 2h shows the magnetic tunnelling gap ($\Delta_{\mathrm{tunnelling}}$) as a function of the ratio between these two crucial momentum quantities, $k_{\mathrm{mag}}/\Delta k_{\mathrm{Weyl}}$. We see that, for $k_{\mathrm{mag}} < \Delta k_{\mathrm{Weyl}}$, the magnetic tunnelling gap is non-observable.

By plugging in the numbers in our case, we see that $k_{\mathrm{mag}} = \Delta k_{W1}$ corresponds to a magnetic field value of 29 T, whereas $k_{\mathrm{mag}} = \Delta k_{W2}$ corresponds to a magnetic field value of 237 T. Remarkably, the magnetic field value corresponding to $k_{\mathrm{mag}} = \Delta k_{W1}$ matches up very well with the observed step-like feature. The Hall signal (see Supplementary Information, proportional to the density of states) shows a peak (dip in $-\sigma_{xy}$) whenever the bottom of a LB (that is, a van Hove singularity (VHS)) crosses the Fermi level. Therefore, $H^* = 34.4$ T corresponds to the magnetic field at which the hybridized LLBs of the W1 Weyl fermions just move above the Fermi level.

We now present systematic temperature and field-angle dependences of the high-field data, which provide further supporting evidence for our observation of the magnetic-field-induced gap
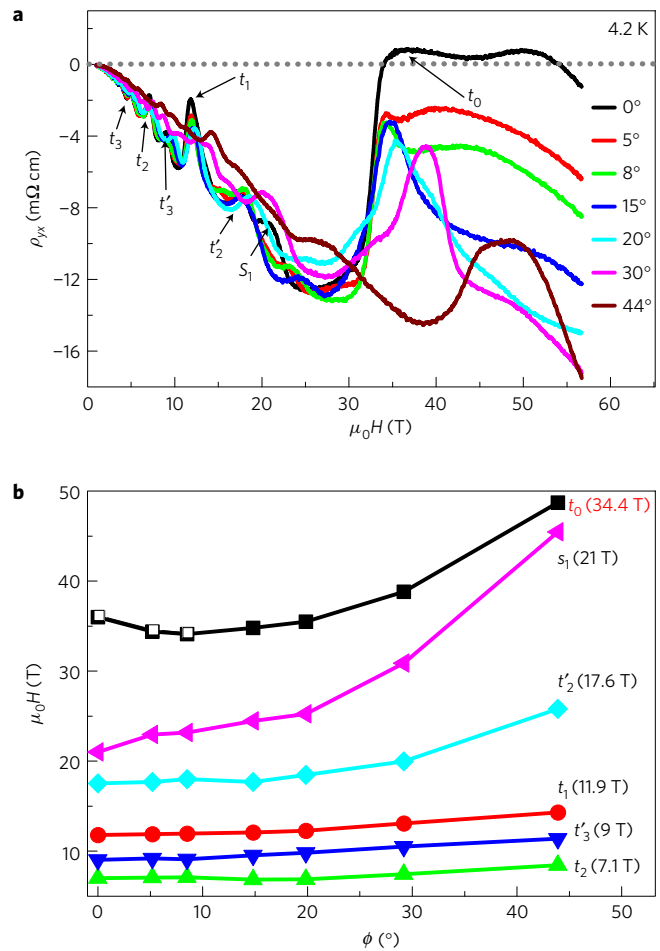

Figure 4 | Magneto-transport of TaP in tilted magnetic fields. **a**, Angle-dependent Hall resistivity ρ_{yx} versus magnetic field $\mu_0 H$ at 4.2 K. At zero degrees (magnetic field being parallel to the $\hat{z}$ direction), there is a sign reversal of ρ_{yx} near the critical field. This sign reversal quickly vanishes with the field being tilted away from the $\hat{z}$ direction. **b**, The field values corresponding to the bottom of the LB crossing E_F as a function of the angle between the magnetic field and the crystalline direction c.

opening and Weyl node annihilation. The ρ_{yx} data at different temperatures are shown in Fig. 3a. The values of H^*, t_1 and t_2 are found to be nearly independent of temperature (Fig. 3e). This is expected because these magnetic fields correspond to the peak of the SdH oscillation data (that is, the bottom of a LB crossing the Fermi level). By contrast, the temperature dependence of Hall resistivity ρ_{yx} at H^* is fairly significant (Fig. 3d).

We found that all SdH peaks (for example, ρ_{yx} at t_2, t_1, and $H^* = t_0$ in Fig. 3a) are strongly temperature dependent. However, the temperature dependence of the higher LBs and the LLB are distinctly different. For a regular SdH peak of a higher Landau band (for example, $t_n \ldots t_3$, t_2, and t_1), we notice the following facts from our data (Fig. 3c): the T-dependence is described well by the 'thermal broadening' $\lambda k_B T /(\sin h(\lambda k_B T))$ (see Supplementary Section IV for more details); on each side of the peak, data at different temperatures form a crossing point; the temperature dependence is roughly symmetric about the SdH peak. By contrast, the T-dependence of the LLB near 34.4 T is different in the following aspects (Fig. 3d): the T-dependence is strongly asymmetric about $H^* = 34.4$ T; only on the left side ($H^* < 34.4$ T), do the data at different temperatures form a crossing point (at about 31.5 T); the asymmetric temperature-dependent behaviour is consistent with the asymmetric band structure of the lowest LB: a regular LB has LBs
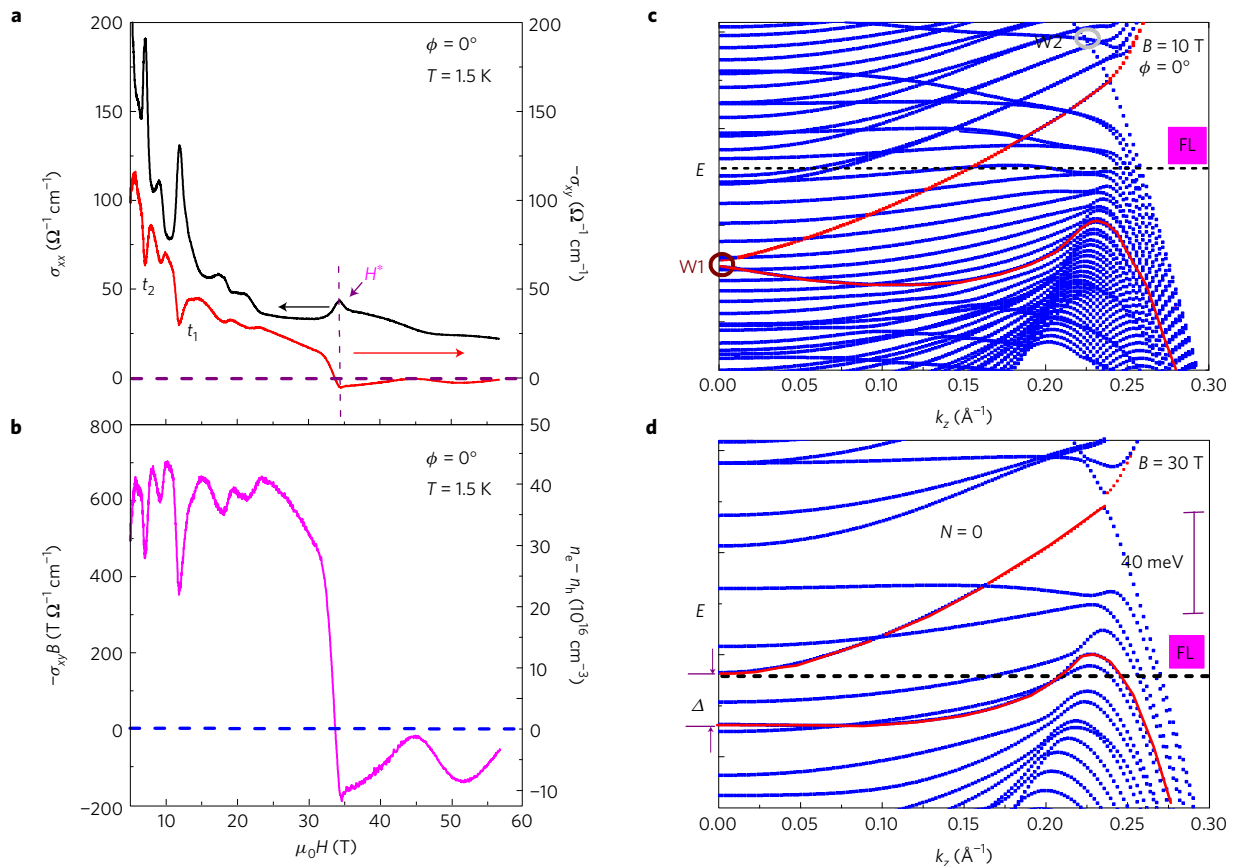
Figure 5 | Conductivity and calculated Landau band structures. a, Field-dependent σ_{xx} and $-\sigma_{xy}$ at 1.5 K. **b**, Field-dependent $\sigma_{xy}B$ from 5 T to 56 T. The scale on the right-hand side gives the quantity of imbalance between holes and electrons. **c,d**, Calculated LB energy dispersion at fields of 10 T and 30 T based on a **k·p** model of TaP, where the physical parameters of model are determined by fitting the model band structure to the first-principles calculated results. The circles (brown for W1, grey for W2) denote locations of Weyl nodes.

both above and below it, whereas the LLB has no further LB below it. The unique temperature dependence near $H^* \sim 34.4$ T proves that the behaviour near $H^* = 34.4$ T cannot be described by the 'thermal broadening' of the regular SdH oscillation alone. In fact, when E_F goes above the bottom of the LLB (that is, for $H > H^*$), we also expect an additional strong temperature dependence from the 'thermal activation', as schematically shown in Fig. 3b. Therefore, to obtain the 'thermal activation gap' for $H > H^*$, we need to remove the 'thermal broadening' effect. In Supplementary Section IV, we describe a method to obtain the 'thermal activation gap'. The obtained gap is shown in Fig. 3g. We see that the gap Δ (between E_F and the bottom of the lowest LB) grows with increasing field. We note that our method still contains approximations (discussions in Supplementary Section IV). Nevertheless, we expect that our analyses capture the essence of the physical process and therefore should give a reasonable estimation of the activation gaps at different H fields.

Figure 4 shows the angle-dependent transport, where the magnetic field is tilted from being parallel to the $\hat{z}$ direction to being parallel to the $\hat{x} + \hat{y}$ direction (in-plane, 45°). The angle dependence data consist of the following two observations: the LBs move to higher magnetic fields as one tilts the field away from the $\hat{z}$ direction; the observed sign reversal quickly vanishes as one tilts the field away from the $\hat{z}$ direction. We note that the first observation is naturally explained by the banana shape of the electron-like pockets, which means that the cross-sectional area of the Fermi surface increases as one tilts the field away from the $\hat{z}$ direction. On the other hand, the second observation provides further supporting evidence for the gap opening. Specifically, considering a pair of Weyl nodes of opposite chirality located on the $k_z = 0$ plane, only a magnetic field

along the $\hat{z}$ direction, B_z, will make the two LLBs cross each other at the same momentum, $k_z = 0$ (see Fig. 2d). This allows the LLBs to hybridize and open up a significant gap at the energy of the Weyl node in a sufficiently large magnetic field. As one tilts the B field away from $\hat{z}$ (keeping in mind that only the momentum along the B field direction is a good quantum number), the LLBs of the Weyl fermions will be separated by a finite momentum at the energy of the Weyl nodes, and they cannot easily hybridize at this energy.

We further obtain the conductivity tensor σ_{xx} and σ_{xy} for $H \parallel c$ from the equations: $\sigma_{xx} = \rho_{xx}/(\rho_{xx}^2 + \rho_{yx}^2)$ and $\sigma_{xy} = \rho_{yx}/(\rho_{xx}^2 + \rho_{yx}^2)$. The Hall conductivity σ_{xy} shows a sharp sign reversal at $H > H^*$ at 1.5 K (Fig. 5a), which is similar to what is being observed in ρ_{yx}. We can estimate the imbalance between electrons and holes by using the equation $\sigma_{xy} = (n_h - n_e)e/B$. It is well known that this equation is valid for a two-band isotropic model. However, in fact, it is also valid for the two-band model in the ultra-quantum limit (see Supplementary Section IV for more details). As shown in Fig. 5b, the carrier imbalance also goes through the steep drop and the sign reversal, signalling a dramatic reduction of the carriers in the Weyl electron pockets. This again provides further evidence for the gap opening for the LLBs of the W1 Weyl fermions in TaP. In Fig. 5c,d, we show the LB spectrum calculations based on a **k·p** model of TaP, where the physical parameters of model are determined by fitting the model band structure to the first-principles calculated results (see Supplementary Section VII for more details). The results of the calculations are consistent with the schematics drawn on the basis of our conceptual arguments (Fig. 2). Specifically, the LBs from the W1 and W2 Weyl fermions are coloured in red and blue, respectively. Indeed we see that at $B = 10$ T, the tunnelling gap is small, which
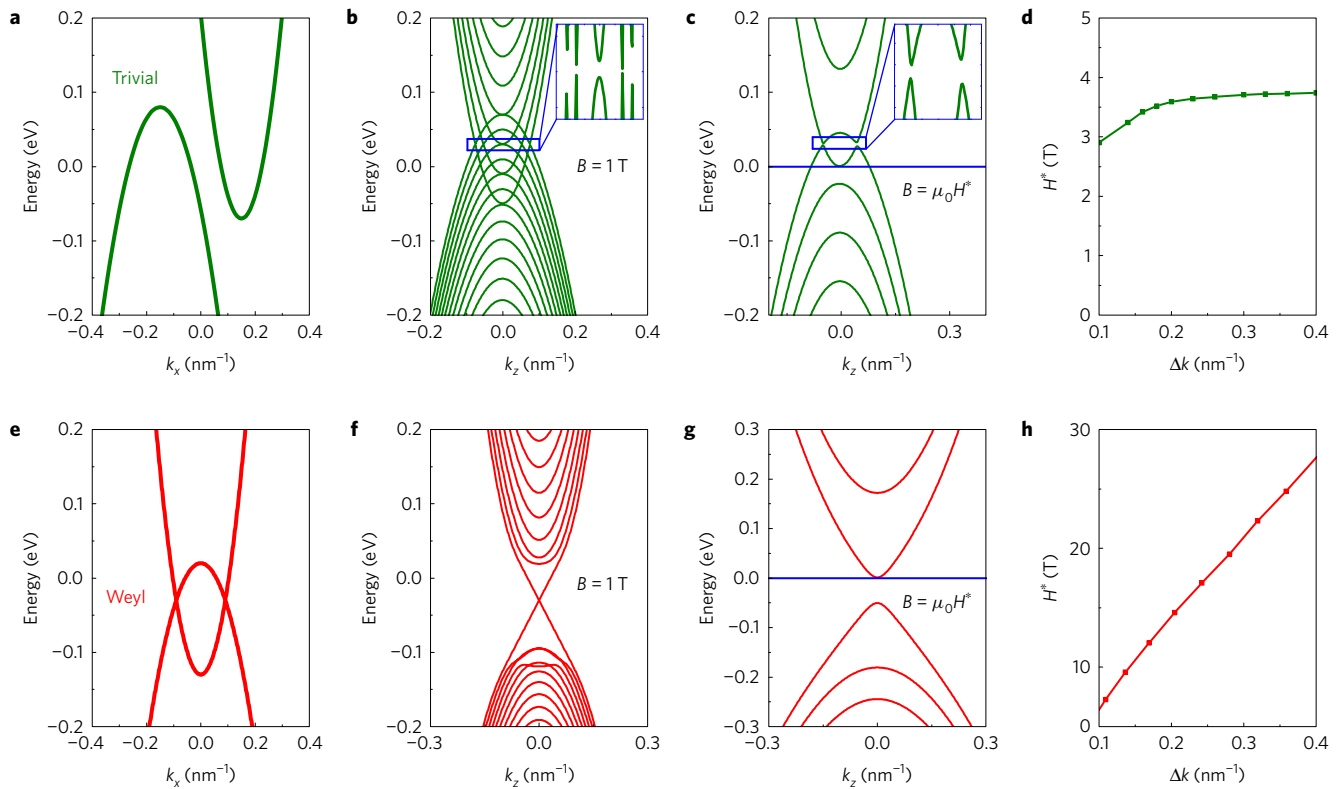
Figure 6 | Comparison between a trivial compensated semimetal and a topological Weyl semimetal. a, Band structure of a trivial compensated semimetal, where an electron-like pocket and a hole-like pocket are separated along k_x. **b,c**, LB structures at different magnetic field values. The magnetic field is along z. A magnetic tunnelling gap opens at all crossing points between the electron-like and hole-like LBs. **d**, H^* (the magnetic field at which the LLB bottom crosses the Fermi level) as a function of Δk (k space separation between the two pockets). **e–h**, The same as **a–d** but for a topological Weyl semimetal. For a trivial compensated semimetal, H^* is mainly dictated by the zero-point energy and therefore shows a minimal dependence on the magnetic tunnelling gap ($\propto \Delta k$). By contrast, for a topological Weyl semimetal, H^* depends solely on the magnetic tunnelling gap and therefore shows a strong dependence on Δk. The parameters: $M_1 = 12.7$ eV nm^2, $M_2 = 6.4$ eV nm^2, $A = 1$ eV nm, $k_w = 0.147$ nm^{-1}, $\mathcal{E} = -0.008$ nm^{-2}, $M_1' = 6.1$ eV nm^2, $M_2' = 12.2$ eV nm^2 and $k_w' = 0.09$ nm^{-1}. In **a**, $\alpha = 0.98$; and in **e**, $\alpha = 0$.

is expected to have no observable effect on the magneto-transport. By contrast, at $B = 30$ T, the tunnelling gap becomes significantly large, leading to the observed sign reversal in our data.

The magnetic-tunnelling-induced Weyl node annihilation in TaP is distinctly different from the magnetic tunnelling effect in topological trivial semimetals. The band structure of the trivial compensated semimetal (Fig. 6a) has an electron-like pocket and a hole-like pocket separated along k_x. (Details of the model can be found in Supplementary Section IX.) With a magnetic field applied along z, the LB spectrum (Fig. 6b) consists of electron-like and hole-like parabolic bands crossing each other. The magnetic tunnelling can open a gap at all the crossing points, which may lead to additional peaks in the quantum oscillation data[31,32]. The magnetic tunnelling gaps in trivial semimetals are away from the tops/bottoms of the parabolic bands. Because the observed H^* corresponds to the bottom of the electron-like LLB crossing the Fermi level, it is mainly dictated by the zero-point energy. We define E_{LLB} as the energy of the bottom of the LLB. We show in Supplementary Information (see Supplementary Fig. 12) that E_{LLB} is nearly independent of Δk. As a result, we see that H^* is also independent of Δk, as shown in Fig. 6d. By contrast, in a Weyl semimetal, H^* depends strongly on Δk because the LLB can move away from the Fermi level only by opening up a magnetic tunnelling gap. We present two critical pieces of evidence in the data: the observed H^* nicely corresponds to $\Delta k_{W1} \sim k_{mag}$; the electron-like pockets (W1) and hole-like pockets (W2) have similar carrier density and similar cyclotron mass. The key difference between them is that k separation between adjacent hole-like pockets is much

larger than that of adjacent electron-like pockets ($\Delta k_{W2} \ll \Delta k_{W1}$). If H^* were solely dictated by the magnetic tunnelling (Δk) like in the Weyl semimetal case, then one would expect to observe the LLBs moving away from E_F only for the electron-like carriers. On the other hand, if H^* were decided only by the zero-point energy $(1/2)\hbar\omega_c$ ($\omega_c = eB/m_c$) like in the trivial case, then one would expect to observe this phenomenon for both carriers. Therefore, the observation in electron-like pockets and non-observation in hole-like pockets reveal the nontrivial topology of Weyl fermions. The magnetic tunnelling observed here is fairly unique in the following aspects. We believe that this is the first observation of a magnetic tunnelling of the LLBs. This is because a Weyl semimetal naturally gives rise to pairs of Fermi pockets with small carrier densities that are close to each other in **k** space. Also, because of the topological character of Weyl fermions, the energy spectrum of their LLBs remains gapless. Except a strong-disorder-induced Anderson localization[33], the magnetic tunnelling is the only way to open a gap so that it can be probed at the Fermi level. Just like previous important findings at high fields[6–13], our work revealed another interesting phenomenon associated with the LLB, that is, magnetic-tunnelling-induced Weyl node annihilation, which paves the way for studying nontrivial topology in electron band structures in other materials.

Methods
Methods, including statements of data availability and any associated accession codes and references, are available in the online version of this paper.

References

1. Klitzing, K. v., Dorda, G. & Pepper, M. New method for high-accuracy determination of the fine-structure constant based on quantized Hall resistance. *Phys. Rev. Lett.* **45,** 494–497 (1980).
2. Tsui, D. C., Stormer, H. L. & Gossard, A. C. Two-dimensional magnetotransport in the extreme quantum limit. *Phys. Rev. Lett.* **48,** 1559–1562 (1982).
3. Yang, K., Haldane, F. D. M. & Rezayi, E. H. Wigner crystals in the lowest Landau level at low-filling factors. *Phys. Rev. B* **64,** 081301 (2001).
4. Staromlynska, J., Finlayson, D. M. & Stradling, R. A. Shubnikov–de Haas measurements in indium antimonide. *J. Phys. C* **16,** 6373–6386 (1983).
5. Zheng, G. *et al.* Transport evidence for the three-dimensional Dirac semimetal phase in ZrTe$_5$. *Phys. Rev. B* **93,** 115414 (2016).
6. *Physics in High Magnetic Fields* (eds Chikazumiand, S. & Miura, N.) (Springer, 1981).
7. Behnia, K., Balicas, L. & Kopelevich, Y. Signatures of electron fractionalization in ultraquantum bismuth. *Science* **317,** 1729–1731 (2007).
8. Li, L. *et al.* Phase transitions of Dirac electrons in bismuth. *Science* **321,** 547–550 (2008).
9. Zhang, C.-L. *et al.* Ultraquantum magnetoresistance in single-crystalline β-Ag$_2$Se. Preprint at http://arxiv.org/abs/1502.02324 (2015).
10. Iye, Y. *et al.* High-magnetic-field electronic phase transition in graphite observed by magnetoresistance anomaly. *Phys. Rev. B* **25,** 5478–5485 (1982).
11. Fauqué, B. *et al.* Two phase transitions induced by a magnetic field in graphite. *Phys. Rev. Lett.* **110,** 266601 (2013).
12. Grüner, G. The dynamics of charge-density waves. *Rev. Mod. Phys.* **60,** 1129–1181 (1988).
13. Fauqué, B., Vignolle, B., Proust, C., Issi, J.-P. & Behnia, K. Electronic instability in bismuth far beyond the quantum limit. *New J. Phys.* **11,** 113012 (2009).
14. Zhu, Z. *et al.* Emptying Dirac valleys in bismuth by magnetic field. Preprint at http://arxiv.org/abs/1608.06199 (2016).
15. Weyl, H. Elektron und gravitation. I. *Z. Phys.* **56,** 330–352 (1929).
16. Herring, C. Accidental degeneracy in the energy bands of crystals. *Phys. Rev.* **52,** 365–373 (1937).
17. Murakami, S. Phase transition between the quantum spin Hall and insulator phases in 3D: emergence of a topological gapless phase. *New J. Phys.* **9,** 356 (2007).
18. Wan, X., Turner, A. M., Vishwanath, A. & Savrasov, S. Y. Topological semimetal and Fermi-arc surface states in the electronic structure of pyrochlore iridates. *Phys. Rev. B* **83,** 205101 (2011).
19. Burkov, A. A. & Balents, L. Weyl semimetal in a topological insulator multilayer. *Phys. Rev. Lett.* **107,** 127205 (2011).
20. Huang, S. M. *et al.* A Weyl fermion semimetal with surface Fermi arcs in the transition metal monopnictide TaAs class. *Nat. Commun.* **6,** 7373 (2015).
21. Weng, H. *et al.* Weyl semimetal phase in non-centrosymmetric transition-metal monophosphides. *Phys. Rev. X* **5,** 011029 (2015).
22. Xu, S.-Y. *et al.* Discovery of a Weyl fermion semimetal and topological Fermi arcs. *Science* **349,** 613–617 (2015).
23. Lv, B. Q. *et al.* Experimental discovery of Weyl semimetal TaAs. *Phys. Rev. X* **5,** 031013 (2015).
24. Xu, S.-Y. *et al.* Discovery of a Weyl fermion state with Fermi arcs in niobium arsenide. *Nat. Phys.* **11,** 748–754 (2015).
25. Zhang, C.-L. *et al.* Electron scattering in tantalum monoarsenide. *Phys. Rev. B* **95,** 085202 (2017).
26. Xu, S.-Y. *et al.* Experimental discovery of a topological Weyl semimetal state in TaP. *Sci. Adv.* **1,** e1501092 (2015).
27. Zhang, C.-L. *et al.* Large magnetoresistance over an extended temperature regime in monophosphides of tantalum and niobium. *Phys. Rev. B* **92,** 041203(R) (2015).
28. Abrikosov, A. A. Quantum magnetoresistance. *Phys. Rev. B* **58,** 2788–2794 (1998).
29. Wang, C. M., Lu, H. Z. & Shen, S. Q. Anomalous phase shift of quantum oscillations in 3D topological semimetals. *Phys. Rev. Lett.* **117,** 077201 (2016).
30. Lu, H. Z., Zhang, S. B. & Shen, S. Q. High-field magnetoconductivity of topological semimetals with short-range potential. *Phys. Rev. B* **92,** 045203 (2015).
31. Cohen, M. H. & Falicov, L. M. Magnetic breakdown in crystals. *Phys. Rev. Lett.* **7,** 231–233 (1961).
32. Sasaki, T., Sato, H. & Toyota, N. Magnetic breakdown effect in organic superconductor κ-(BEDT-TTF)$_2$Cu(NCS)$_2$. *Solid State Commun.* **76,** 507–510 (1990).
33. Chen, C.-Z. *et al.* Disorder and metal-insulator transitions in Weyl semimetals. *Phys. Rev. Lett.* **115,** 246603 (2015).

Author contributions

C.-L.Z. and S.J. designed the experiment. C.-L.Z. performed all electrical transport experiments with help from Z.L., C.G., H.Lu, Y.F., L.L., C.Z., J.Z., J.W. and S.J.; S.-Y.X. conducted ARPES experiments with assistance from M.Z.H.; C.-L.Z., C.G., H.Lu and Y.F. grew the single-crystal samples; C.-C.L., G.C., S.-M.H., C.-H.H. and H.Lin performed first-principles band structure calculations; C.M.W., Z.Z.D. and H.-Z.L. did all theoretical simulations and part of theoretical analyses; Z.Z.D. and H.-Z.L. proposed the two-band model for trivial and Weyl semimetals. H.Liu and X.-C.X. contributed the Landau band indexation. S.-M.H. also performed Landau level simulations. T.N. performed the major part of theoretical analyses and gave the $k \cdot p$ model. S.-Y.X., C.-L.Z., C.M.W., H.-Z.L., T.N. and S.J. wrote the paper. S.-Y.X. and S.J. were responsible for the overall direction, planning and integration among different research units.

Additional information

Supplementary information is available in the online version of the paper. Reprints and permissions information is available online at www.nature.com/reprints. Publisher's note: Springer Nature remains neutral with regard to jurisdictional claims in published maps and institutional affiliations. Correspondence and requests for materials should be addressed to H.-Z.L., J.W. or S.J.

Competing financial interests

The authors declare no competing financial interests.

Methods

Single crystals of TaP were prepared and characterized as described in ref. 27. Magneto-transport measurements in fields up to 56 T were performed at the Wuhan National High Magnetic Field Center. A Digital lock-in technique was employed with a 100 kHz frequency and a 5 mA excitation current by using a non-destructive pulse magnet with a pulse duration of 60 ms. Magneto-resistance and Hall resistance were measured simultaneously with a typical five-probe method. To eliminate the effects of contact asymmetries, measurements with both positive and negative field polarities were made for all temperatures and angular positions. Data for the up-sweeping and down-sweeping of the pulse field were in good agreement, and we can thus exclude the self-heating effect of the sample in the pulsed high magnetic fields. The de Haas–van Alphen measurements were carried out in a pulsed field at the National High Magnetic Field Laboratory in Los Alamos (NHMFL, LANL).

First-principles calculations were performed by the OPENMX code within the framework of the generalized gradient approximation of density functional theory[34], as discussed in detail in ref. 20. The soft X-ray ARPES (SX-ARPES) measurements were performed at the ADRESS Beamline at the Swiss Light Source in the Paul Scherrer Institut in Villigen, Switzerland using photon energies ranging from 300 to 1,000 eV (ref. 35). The energy and angle resolutions were better than 80 meV and 0.07°, respectively. Samples were cleaved *in situ* under a vacuum condition better than 5×10^{-11} torr, resulting in shiny and flat surfaces. The measurements were performed at a temperature of approximately 15 K.

References

34. Perdew, J. P., Burke, K. & Ernzerhof, M. Generalized gradient approximation made simple. *Phys. Rev. Lett.* **77,** 3865–3868 (1996).
35. Strocov, V. N. *et al*. Soft-X-ray ARPES facility at the ADRESS beamline of the SLS: concepts, technical realisation and scientific applications. *J. Synchrotron Radiat.* **21,** 32–44 (2014).